Holey sheets: Double-Threshold Rupture of Draining Liquid Films

Ayush K. Dixit,[1,*] Chunheng Zhao,[2,†] Stéphane Zaleski,[3,4,‡] Detlef Lohse,[1,5,§] and Vatsal Sanjay[6,1,¶]

[1] *Physics of Fluids Department, Max Planck Center Twente for Complex Fluid Dynamics, and J. M. Burgers Center for Fluid Dynamics, University of Twente, P.O. Box 217, 7500AE Enschede, Netherlands*

[2] *Department of Mechanical Engineering, City College of New York, New York, New York 10031, USA*

[3] *Sorbonne Université and CNRS, UMR 7190, Institut Jean Le Rond ∂'Alembert, 75005 Paris, France*

[4] *Institut Universitaire de France, UMR 7190, Institut Jean Le Rond ∂'Alembert, 75005 Paris, France*

[5] *Max Planck Institute for Dynamics and Self-Organisation, Am Fassberg 17, 37077 Göttingen, Germany*

[6] *CoMPhy Lab, Department of Physics, Durham University, Science Laboratories, South Road, Durham DH1 3LE, United Kingdom*

(Dated: September 21, 2025)

Classical rupture is attributed to molecular (van der Waals) forces acting at nanometric thicknesses. Nonetheless, micron-thick liquid sheets routinely perforate far above the scale where these molecular forces act, yet the mechanism that selects opening versus healing has remained unclear. Using direct numerical simulations of a draining sheet with an entrained air bubble (cavity), we show that irreversible rupture occurs only when a deterministic double-threshold is crossed: (i) the outward driving (from airflow or inertia) is strong enough and (ii) the cavity is distorted enough. If either condition falls short, surface tension heals the cavity and the sheet reseals. The time for this process is set by the balance between inertia and viscosity – fast for inertia-dominated sheets and slower for viscous ones. This double-threshold mechanism explains why micrometer-thick films perforate and offers practical control options – driving strength and defect geometry – for predicting and controlling breakup in spray formation processes, wave breaking, and respiratory films.

The rupture of thinning liquid sheets is a ubiquitous route to fluid fragmentation, underlying phenomena from respiratory aerosolization to agricultural sprays and wave breaking [1]. During the recent COVID-19 pandemic [2], the public became acutely aware of how violent expiratory events such as coughing and sneezing produce virus-laden droplets. High-speed visualization of real-life coughs [3–5], and experiments with mechanical cough devices [6, 7] show that a mucosalivary liquid layer in the respiratory tract can be sheared into a thin bag-like sheet that drains and thins rapidly. Eventually, holes appear spontaneously in these thinning sheets, which expand and cause the sheet to break apart, resulting in a cloud of droplets. Similar sheet rupture and drop-formation processes occur in a variety of contexts, including ocean wave breaking [1], agricultural spray dispersal [8], rain-induced aerosols [9], spray cleaning [10], and drop impact on liquid pools [11, 12] or even solids [13] (fig. 1a). Quantifying how such droplets are generated is crucial for accurate risk assessments of airborne disease transmission [4], optimizing pesticide applications [8], and quantifying sea spray aerosol generation [14].

A key step in all of these processes is the nucleation of holes in the thinning sheet, which sets the eventual droplet size distribution [15, 16]. However, despite its ubiquity, the physical origin of these holes remains debated [17] – especially for micrometer-thick sheets, where molecular mechanisms (van der Waals forces or thermal fluctuations) are too weak to explain rupture [18]. Consistent with this view, experiments show that breakup typically occurs once sheets thin to micron scales and that holes nucleate at internal defects – entrained bubbles or oil droplets – within the sheet [6, 11, 19–22]. In particular, bubbles in so-called Savart water sheets produced by a jet impinging on a disk have been observed to perforate the sheet [23, 24]. Yet the pathway by which a bubble or other impurity triggers hole formation—particularly under realistic sheet-drainage conditions—remains unresolved because the nucleation events are rapid and difficult to control and visualize.

In this Letter, we show that an air bubble entrained in a draining liquid sheet can nucleate a hole long before molecular-scale forces become relevant. Axisymmetric direct numerical simulations performed with the Navier-Stokes and combined level-set-volume-of-fluid solver Basilisk C [25, 26] isolate this impurity-driven pathway under controlled conditions while retaining realistic rim dynamics. To focus on the essential physics, we replace the inflating bag geometry of air-blast breakup by an initially flat sheet of thickness h_0 that drains radially with $u(r) = \omega r$ (fig. 1b), a template that captures both external-airflow forcing in bag breakup [38] and inertia-driven drainage after drop impact [39]. The dynamics are governed by the Ohnesorge number $Oh = \eta/\sqrt{\rho\gamma R_0}$, the Bond number $Bo = \rho\omega^2 R_0^3/\gamma$, and the non-dimensionlized offset χ/R_0 of the bubble's center from the centerlines of the flow. Here η and ρ are the liquid viscosity and density, γ is the surface tension, and R_0 the bubble radius. The driving acceleration $\omega^2 R_0$ acts as an effective radial gravity. In addition, the initial cavity distortion is characterized by an open angle θ (fig. 1c), see supplementary material [26] for details on drainage mechanism leading to this geometry.

Our two key results are as follows: First, the entrained bubble grows a through-cavity that overcomes surface tension and nucleates a hole at micrometer-scale thicknesses, explaining rupture without invoking nanoscale physics. Second, the post-nucleation fate is deterministic and requires crossing a double-threshold for irreversible opening: the outward drainage must exceed a critical $Bo_c(Oh)$ and the initial cavity distortion – characterized by an opening angle θ – must exceed a critical $\theta_c(Oh)$. Otherwise, rims collide and the sheet heals. The opening-healing boundary collapses onto simple asymptotic scalings: $Bo_c = \mathcal{O}(1)$ for $Oh \ll 1$ and $Bo_c \sim Oh^{-2}$ for $Oh \gg 1$. These results rationalize the observed perforation of micron-thick sheets by internal defects and provide a predictive framework for impurity-induced breakup in natural and engineered fragmentation flows.

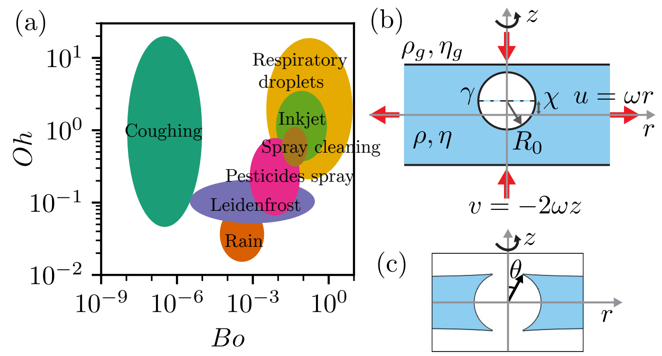

FIG. 1. (a) Liquid sheets characterized by control parameters Oh and Bo are relevant in several phenomena across the entire parameter space. (b) Schematic side view of a liquid sheet that is radially draining and, subsequently, thinning along the axial direction. The flow directions of the liquid are indicated in red. A bubble with radius R_0 is placed axisymmetrically but offset axially by a distance χ. (c) When additional physical factors delay the nucleation of the hole, the initial conditions used in simulations are characterized by the polar angle θ made at the cavity edge.

Phenomenology – We first examine sheet-centered bubbles ($\chi/R_0 = 0$) across the (Oh, Bo) space. As the sheet thins, its top and bottom interfaces meet at the bubble poles and a through-cavity opens. Capillary waves invert the cavity from convex to concave, after which two outcomes are observed (fig. 2a,b): either the rims retract and the hole expands, breaking the sheet, or capillarity drives rim collision and the sheet heals. A systematic sweep in (Oh, Bo) reveals a sharp transition curve (fig. 2c): strong radial driving (large Bo) yields opening, whereas weaker driving permits healing unless Bo exceeds a viscosity-dependent threshold. The location and slope of this boundary reflect the competition between capillary-driven rim closure and drainage-driven advection, anticipating the timescale analysis that follows. We additionally show that delayed nucleation–representing chemical/thermal heterogeneity–can be encoded by a larger initial cavity characterized by an opening angle θ, which shifts the transition and thereby introduces geometry as a second way of control.

Relevant timescales set the healing to opening transition – After the bubble's and sheet's interfaces merge and create an initial cavity through the sheet, we measure the time it takes for the two opposing rims to collide at the sheet's central axis; we term this the "collision time" t_c. Physically, t_c represents the healing time when the sheet successfully reseals. Fig. 3(a) shows t_c (normalized by the inertio-capillary timescale $\tau_\gamma = \sqrt{\rho R_0^3/\gamma}$) as a function of Oh for several values of Bo (including Bo just below the opening threshold for each Oh). At low viscosity ($Oh \ll 0.1$), we find that $t_c \sim \tau_\gamma$, insensitive to Oh. At higher viscosity ($Oh \gg 0.1$), $t_c/\tau_\gamma \sim Oh$.

These trends can be understood by considering the dominant balance of forces resisting hole closure. For small Oh (inertia-dominated regime), viscous resistance is negligible and inertial forces dominate. Balancing surface tension and inertia yields a characteristic rim velocity $U_0 \sim \sqrt{\gamma/(\rho R_0)}$ and thus $t_c \sim \tau_\gamma \equiv \sqrt{\rho R_0^3/\gamma}$. In contrast, for large Oh (viscosity-dominated regime), balancing surface tension with viscous stress (of order $\eta U_0/R_0$) gives $U_0 \sim \gamma/\eta$ and hence $t_c \sim \eta R_0/\gamma \sim \tau_\gamma Oh$, a visco-capillary timescale. These scaling predictions agree well with the simulation results in fig. 3(a).

Notably, even when Bo is very close to its critical value $Bo_c(Oh)$ (beyond which the sheet would open), the measured healing time t_c is essentially the same as for much smaller Bo. Thus, while radial driving (Bo) determines whether the sheet ultimately opens or heals, the healing dynamics themselves is primarily controlled by the liquid's inertial-viscous balance (Oh).

We can predict the boundary between opening and healing regimes by comparing the timescales for rim retraction versus radial sheet advection. For the sheet to open, outward advection (driven by ω, with timescale $t_{\mathrm{adv}} \sim 1/\omega$) must outpace capillary-driven rim closure (timescale t_c). At low viscosities (small Oh, where $t_c \sim \tau_\gamma$), the criterion $t_c \sim t_{\mathrm{adv}}$ leads to $\sqrt{\rho R_0^3/\gamma} \sim 1/\omega$, yielding $Bo \sim 1$ in dimensionless terms. At high viscosities (large Oh, where $t_c \sim \eta R_0/\gamma$), the condition $t_c \sim 1/\omega$ gives $Oh \sim Bo^{-1/2}$. These theoretical thresholds – shown as the gray (vertical) and black (diagonal) lines in fig. 2(c) – closely match the transition observed in our simulations.

What happens in the limiting case of no external driving ($Bo = 0$)? – In the absence of radial forcing ($Bo = 0$), the liquid sheet inevitably heals for any finite Oh – even extremely viscous sheets (large Oh) will eventually reseal, albeit very slowly as viscosity prolongs the rim collision time. This follows from our thresholds: as $Bo \to 0$, achieving opening would require $Oh \sim Bo^{-1/2} \to \infty$, so any finite Oh lies in the healing regime. Our simulations confirm this universal healing at $Bo = 0$, consistent with the classic geometric energy criterion of Taylor & Michael [40]. Using a toroidal model for the hole's rim

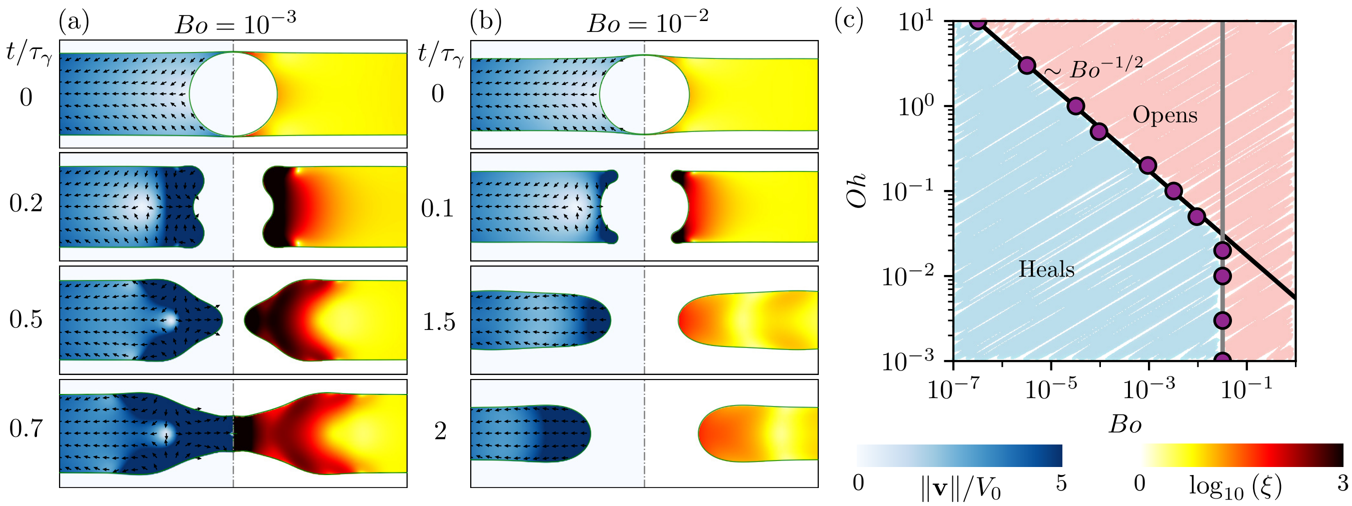

FIG. 2. As the liquid sheet drains radially and thins axially, the interfaces of the bubble and sheet merge to create a cavity. The time instants are shown for $Oh = 0.1$, (a) and at small $Bo = 10^{-3}$ where the sheet heals, while (b) at larger $Bo = 10^{-2}$, the sheet opens up. The left panel depicts velocity magnitude $\|\boldsymbol{v}\|/V_0$, where $V_0 = \sqrt{Bo\gamma/\rho R_0}$, and the black arrows depict the velocity direction. The right panel illustrates viscous dissipation $\xi = 2Bo\left(\boldsymbol{\mathcal{D}} : \boldsymbol{\mathcal{D}}\right)$, where $\boldsymbol{\mathcal{D}} = \left(\boldsymbol{\nabla u} + \boldsymbol{\nabla u}^T\right)/2$ is the symmetric part of velocity gradient tensor. (c) The regime map in the log-log parameter space of $Oh - Bo$. The transition lines at small Oh are shown by a constant Bo line in gray, while, at large Oh, the transition is indicated by a black line with scaling $Oh \sim Bo^{-1/2}$.

[41], they predicted that without external driving a circular hole can continue to expand only if its radius exceeds a purely geometric threshold. In particular, when the hole's outer radius R satisfies $R/h_0 > \pi/4$ (so that the inner radius $R_h = R - h_0/2$ is about $0.29h_0$), the excess surface energy $\Delta\Xi$ becomes positive, signaling that the hole will grow rather than close. Holes smaller than this critical size have $\Delta\Xi < 0$ and will heal. Notably, this threshold is independent of viscosity. Thus, at $Bo = 0$ no finite-Oh case can open unless the initial hole is above the critical R/h_0 – indeed, the cavities in our simulations were below this size, so they all heal.

In more realistic situations, additional physics can delay the initial rupture (for example, due to chemical or thermal heterogeneity), allowing the sheet to drain longer and thin more broadly before the hole forms. We represent such delays in our model by a larger initial cavity distortion characterized by an increased polar angle θ (fig. 1c). Simulations at $Bo = 0$ with varied θ reveal a clear geometry-controlled threshold: for sufficiently large distortions (large θ), the hole opens even without any driving, whereas for smaller initial distortions the hole heals (fig. 3b). This confirms the second threshold of the double-threshold framework: a sufficiently large initial cavity alone can trigger sheet rupture in the absence of external forcing. Moreover, at very high viscosity (large Oh), the opening-healing transition occurs at a nearly constant $\theta \approx 0.09\pi$, consistent with the $R_h/h_0 \approx 0.29$ criterion seen in our simulations at large Oh. As Oh decreases (inertia-dominated regime), this critical distortion θ_c rises, since added inertia aids rim closure—requiring a larger initial opening to overcome healing. Remarkably, sheets that do open exhibit non-monotonic cavity growth (fig. 3c). Surface tension first drives the cavity edges apart, causing radial cavity growth, but the induced inertia pulls the rim inward and temporarily reduces the cavity radius. However, the cavity remains large enough to overcome healing by this recoil and eventually opens with the Taylor–Culick mechanism.

Effect of off-center bubbles – Thus far we considered sheet-centered bubbles ($\chi/R_0 = 0$) with simultaneous holes at both poles; in practice, an off-center bubble ($\chi/R_0 \neq 0$) breaks this symmetry. For $\chi/R_0 > 0$, only the thinner pole ruptures initially, leaving a draining liquid bridge at the opposite pole. If the offset is very small ($\chi \to 0$), that remaining bridge is extremely thin and often ruptures almost immediately due to van der Waals forces – essentially the symmetric outcome. For moderate asymmetry, however, the first opening launches a capillary wave that travels toward the far pole and drives fluid into the intact bridge (fig. 4), temporarily replenishing it and suppressing prompt hole nucleation there – unlike the symmetric case (fig. 4a).

Nonetheless, even without an immediate second hole, the bubble's presence can significantly shorten the sheet's lifetime, especially at high Oh. At low viscosity (small Oh) and weak driving, the capillary wave significantly thickens the far-side liquid bridge, so the sheet drains nearly as if no bubble were present (fig. 4a). In this regime the bubble has minimal effect on the breakup time. At higher viscosity (large Oh), however, capillary

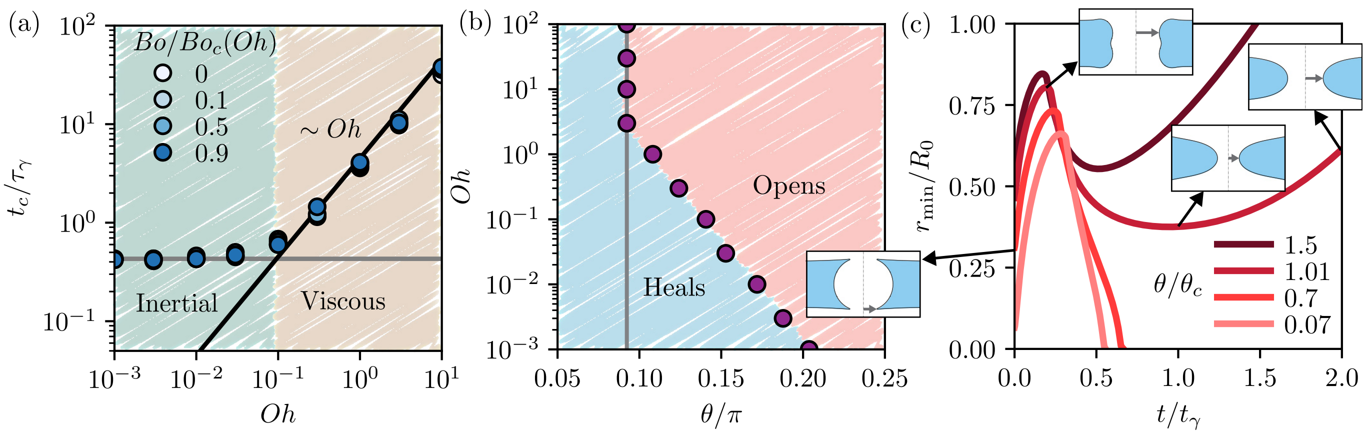

FIG. 3. (a) After the bubble cavity opens, in some cases, capillarity manages to heal the rims, and the time taken is referred to as the collision time t_c. Here, t_c/τ_γ is plotted against Oh at several Bo, where $\tau_\gamma = \sqrt{\rho R_0^3/\gamma}$. At small Oh, the gray line shows the scaling of the inertio-capillary timescale, while the black line shows the visco-capillary time scale at large Oh; both scalings seem to be consistent with simulation results. (b) The parameter space of $Oh - \theta$ highlighting the healing and opening regimes with different colors. The gray line shows the transition observed at $\theta = 0.09\pi$ at large Oh, while the individual data points are also denoted. (c) The evolution of minimum tip radius $r_{\min}$ at several initial distortions θ for $Oh = 0.1$ without external driving. For smaller distortions, $r_{\min}$ decays to zero, whereas for larger distortions, sheets eventually open irreversibly, consistent with Taylor-Culick retractions. At several instances, the insets depict sheet profiles and highlight $r_{\min}$ with gray arrows.

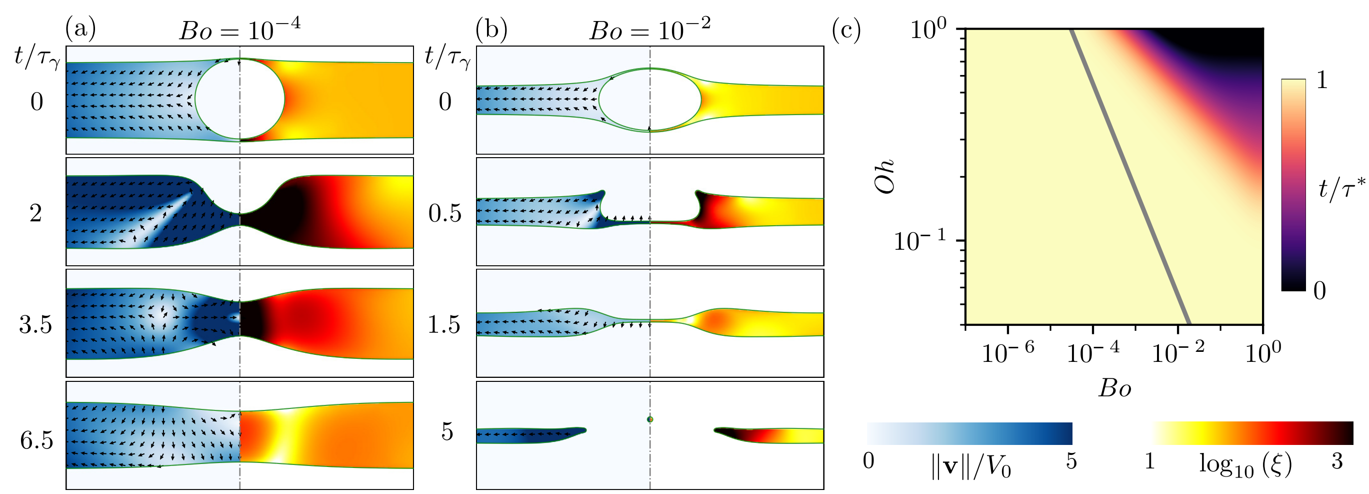

FIG. 4. The draining liquid sheet of the bubble is placed asymmetrically with $\chi/R_0 = 0.1$. Time evolution has been shown for cases with $Oh = 1$, (a) $Bo = 10^{-4}$, and (b) $Bo = 10^{-2}$. In the former case, the liquid bridge at the south pole replenishes and grows into a flat-shaped sheet due to capillary action, and then the sheet keeps on thinning due to radial drainage. Meanwhile, in the latter case, thinning due to radial drainage dominates before the bridge can be replenished by the damped capillary waves at large $Oh = 1$. The left panel depicts velocity magnitude $\|\boldsymbol{v}\|/V_0$, where $V_0 = \sqrt{Bo\gamma/\rho R_0}$, the black arrows depict the velocity direction. The right panel depicts viscous dissipation $\xi = 2Bo\left(\boldsymbol{\mathcal{D}} : \boldsymbol{\mathcal{D}}\right)$, where $\boldsymbol{\mathcal{D}} = \left(\boldsymbol{\nabla u} + \boldsymbol{\nabla u}^T\right)/2$ is the symmetric part of velocity gradient tensor. (c) Sheet breakup time (normalized by the no-bubble case rupture time $\tau^* \sim \tau_\gamma/\sqrt{Bo}$) in the $Oh - Bo$ parameter space for $\chi/R_0 = 0.1$. The gray line depicts the transition line observed for symmetric cases ($\chi/R_0 = 0$), as shown in fig. 2.

replenishment is strongly damped; the bridge thins continuously under drainage and ruptures much earlier than it would in a sheet without bubble (fig. 4b). Fig. 4(c) quantifies these trends by mapping the sheet breakup time (normalized by the no-bubble value τ^*) across the Oh-Bo parameter space for $\chi = 0.1R_0$. Consistent with the above description, the bubble significantly hastens breakup in the high-Oh, high-Bo regime (dark regions), whereas at low Oh/low Bo the breakup time is nearly unchanged from the bubble-free case (light regions). Comparing to the symmetric configuration (gray transition line from fig. 2), we see that an off-center bubble is generally less effective at triggering rupture: with one pole's bridge intact, the sheet is less prone to instantaneous rupture, and the parameter region of strong bubble influence is reduced. In the limit of vanishing asymmetry, the behavior converges to the symmetric case (points approaching the gray line in fig. 4c). Further analysis of varying χ is provided in [26].

Conclusion & Outlook – We have shown that a micron-thick draining sheet pierced by a trapped bubble undergoes irreversible rupture only if a double-threshold is exceeded: the driving (e.g., airflow or inertia) must exceed a critical Bond number $Bo_c(Oh)$, and the initial cavity distortion – captured by a geometric opening angle θ – must exceed a threshold $\theta_c(Oh)$. If either threshold is unmet, capillarity heals the sheet on an inertio- ($Oh \ll 1$) or visco-capillary ($Oh \gg 1$) timescale. This double-threshold mechanism is reminiscent of hole formation in drops impacting on rough surfaces, where a sufficiently high inertia and a large surface roughness are both required for holes to nucleate [13, 17, 46]. Similar double-thresholds govern other nonlinear transitions in fluids: for example, turbulence in shear flow develops only when the Reynolds number is high and the initial perturbation amplitude is large [47], and elastic turbulence in polymer solutions likewise demands a large Weissenberg number together with strong disturbances [48]. Importantly, an isolated flat liquid sheet in air is linearly stable as small distortions decay and rupture only occurs through finite amplitude distortions [49–53]. This nonlinearity of the healing–opening transition is reflected in our simulations, where small initial cavities decay while sufficiently large ones rupture (fig. 3c). However, unlike the subcritical double-threshold mechanism behavior in transition to turbulence, our system is not subcritical and thus not hysteretic: once parameters (Bo, θ, Oh) are set, the outcome (healing or opening) is uniquely determined.

A trapped bubble – acting as a hydrophobic defect – thus rationalizes why rupture occurs far above molecular scales and provides predictive control knobs, namely driving strength and defect geometry, relevant to bag-breakup sprays and respiratory films. Future studies could test whether analogous thresholds govern rupture triggered by solid particles, oil droplets, or Marangoni-driven inhomogeneities. Chemical or thermal gradients may couple nonlinearly with radial drainage and shift $Bo_c(Oh)$ and $\theta_c(Oh)$, extending this double-threshold framework to a broader class of impurity-triggered, geometry-sensitive instabilities.

Acknowledgments: We acknowledge the funding from the MIST consortium with project number P20-35 of the research programme Perspectief, which is (partly) financed by the Dutch Research Council (NWO). We also acknowledge the NWO-Canon grant FIP-II grant. This work was carried out on the national e-infrastructure of SURFsara, a subsidiary of SURF cooperation, the collaborative ICT organization for Dutch education and research. This work was sponsored by NWO - Domain Science for the use of supercomputer facilities. Stéphane Zaleski and Chunheng Zhao were funded by the European Research Council (ERC) through the European Union's Horizon 2020 Research and Innovation Programme (Grant Agreement No. 883849 TRUFLOW).

* a.k.dixit@utwente.nl
† czhao000@citymail.cuny.edu
‡ stephane.zaleski@sorbonne-universite.fr
§ d.lohse@utwente.nl
¶ vatsal.sanjay@comphy-lab.org

[1] L. Deike, *Mass transfer at the ocean–atmosphere interface: the role of wave breaking, droplets, and bubbles*, Annu. Rev. Fluid Mech. **54**, 191 (2022).

[2] M. Ciotti, M. Ciccozzi, A. Terrinoni, W.-C. Jiang, C.-B. Wang, and S. Bernardini, *The COVID-19 pandemic*, Crit. Rev. Clin. Lab. Sci. **57**, 365 (2020).

[3] B. E. Scharfman, A. H. Techet, J. W. M. Bush, and L. Bourouiba, *Visualization of sneeze ejecta: steps of fluid fragmentation leading to respiratory droplets*, Exp. Fluids **57**, 1 (2016).

[4] L. Bourouiba, *The fluid dynamics of disease transmission*, Annu. Rev. Fluid Mech. **53**, 473 (2021).

[5] M. L. Pöhlker, C. Pöhlker, O. O. Krüger, J.-D. Förster, T. Berkemeier, W. Elbert, J. Fröhlich-Nowoisky, U. Pöschl, G. Bagheri, E. Bodenschatz, *et al.*, *Respiratory aerosols and droplets in the transmission of infectious diseases*, Rev. Mod. Phys. **95**, 045001 (2023).

[6] P. Kant, C. Pairetti, Y. Saade, S. Popinet, S. Zaleski, and D. Lohse, *Bag-mediated film atomization in a cough machine*, Phys. Rev. Fluids **8**, 074802 (2023).

[7] M. Li, Y. Saade, S. Zaleski, U. Sen, P. Kant, and D. Lohse, *Viscoelasticity reduces the droplet size in mucosalivary film fragmentation during intense respiratory events*, Phys. Rev. Fluids **10**, 084001 (2025).

[8] I. Makhnenko, E. R. Alonzi, S. A. Fredericks, C. M. Colby, and C. S. Dutcher, *A review of liquid sheet breakup: Perspectives from agricultural sprays*, J. Aerosol Sci. **157**, 105805 (2021).

[9] E. Villermaux and B. Bossa, *Single-drop fragmentation determines size distribution of raindrops*, Nature Phys. **5**, 697 (2009).

[10] C. Josserand and S. T. Thoroddsen, *Drop impact on a solid surface*, Annu. Rev. Fluid Mech. **48**, 365 (2016).

[11] A. B. Aljedaani, C. Wang, A. Jetly, and S. T. Thoroddsen, *Experiments on the breakup of drop-impact crowns by Marangoni holes*, J. Fluid Mech. **844**, 162 (2018).

[12] H. Lhuissier, C. Sun, A. Prosperetti, and D. Lohse, *Drop fragmentation at impact onto a bath of an immiscible liquid*, Phys. Rev. Lett. **110**, 264503 (2013).

[13] S. Kim, Z. Wu, E. Esmaili, J. J. Dombroskie, and S. Jung, *How a raindrop gets shattered on biological surfaces*, Proc. Natl. Acad. Sci. USA **117**, 13901 (2020).

[14] G. De Leeuw, E. L. Andreas, M. D. Anguelova, C. W. Fairall, E. R. Lewis, C. O'Dowd, M. Schulz, and S. E. Schwartz, *Production flux of sea spray aerosol*, Rev. Geophys. **49**, (2011).

[15] N. Dombrowski and R. P. Fraser, *A photographic inves-*

tigation into the disintegration of liquid sheets, Philos. Trans. R. Soc. A **247**, 101 (1954).
[16] G. I. Taylor, *The dynamics of thin sheets of fluid. III. Disintegration of fluid sheets*, Proc. R. Soc. A **253**, 313 (1959).
[17] D. Lohse and E. Villermaux, *Double threshold behavior for breakup of liquid sheets*, Proc. Natl. Acad. Sci. USA **117**, 18912 (2020).
[18] B. Néel and E. Villermaux, *The spontaneous puncture of thick liquid films*, J. Fluid Mech. **838**, 192 (2018).
[19] L. Opfer, I. V. Roisman, J. Venzmer, M. Klostermann, and C. Tropea, *Droplet-air collision dynamics: Evolution of the film thickness*, Phys. Rev. E **89**, 013023 (2014).
[20] I. M. Jackiw and N. Ashgriz, *On aerodynamic droplet breakup*, J. Fluid Mech. **913**, A33 (2021).
[21] B. Stumpf, I. V. Roisman, A. L. Yarin, and C. Tropea, *Drop impact onto a substrate wetted by another liquid: corona detachment from the wall film*, J. Fluid Mech. **956**, A10 (2023).
[22] S. T. Thoroddsen, T. G. Etoh, and K. Takehara, *Crown breakup by Marangoni instability*, J. Fluid Mech. **557**, 63 (2006).
[23] H. Lhuissier and E. Villermaux, *'Effervescent'atomization in two dimensions*, J. Fluid Mech. **714**, 361 (2013).
[24] C. Gong, D. Li, and C. Kang, *Effect of oil-based emulsion on air bubbles in the spray sheet produced through the air-induction nozzle*, Pest Manag. Sci. **78**, 5347 (2022).
[25] S. Popinet and collaborators, Basilisk C, `http://basilisk.fr` (Last accessed: April, 2025), 2013–2025.
[26] See Supplemental Material at (URL to be inserted by the publisher) for a description of the governing equations, numerical method, initial shape effects and asymmetry effects, which includes Refs. [27–37], 2025.
[27] A. K. Dixit and V. Sanjay, Code repository: Holey Sheets, https://github.com/comphy-lab/HoleySheet, 2025.
[28] G. Tryggvason, R. Scardovelli, and S. Zaleski, *Direct Numerical Simulations of Gas–Liquid Multiphase Flows* (Cambridge University Press, ADDRESS, 2011).
[29] J. U. Brackbill, D. B. Kothe, and C. Zemach, *A continuum method for modeling surface tension*, J. Comput. Phys. **100**, 335 (1992).
[30] M. Sussman and E. G. Puckett, *A coupled level set and volume-of-fluid method for computing 3D and axisymmetric incompressible two-phase flows*, J. Comput. Phys. **162**, 301 (2000).
[31] M. Saini, V. Sanjay, Y. Saade, D. Lohse, and S. Popinet, *Implementation of integral surface tension formulations in a volume of fluid framework and their applications to Marangoni flows*, arXiv preprint arXiv:2502.02712 (2025).
[32] S. Popinet, *A quadtree-adaptive multigrid solver for the Serre–Green–Naghdi equations*, J. Comput. Phys. **302**, 336 (2015).
[33] S. Popinet, *An accurate adaptive solver for surface-tension-driven interfacial flows*, J. Comput. Phys. **228**, 5838 (2009).
[34] S. Popinet, *Numerical models of surface tension*, Annu. Rev. Fluid Mech. **50**, 49 (2018).
[35] L. Duchemin, S. Popinet, C. Josserand, and S. Zaleski, *Jet formation in bubbles bursting at a free surface*, Phys. Fluids **14**, 3000 (2002).
[36] L. Deike, E. Ghabache, G. Liger-Belair, A. K. Das, S. Zaleski, S. Popinet, and T. Séon, *Dynamics of jets produced by bursting bubbles*, Phys. Rev. Fluids **3**, 013603 (2018).
[37] W. Bouwhuis, R. C. A. van der Veen, T. Tran, D. L. Keij, K. G. Winkels, I. R. Peters, D. van der Meer, C. Sun, J. H. Snoeijer, and D. Lohse, *Maximal air bubble entrainment at liquid-drop impact*, Phys. Rev. Lett. **109**, 264501 (2012).
[38] M. Jalaal and K. Mehravaran, *Fragmentation of falling liquid droplets in bag breakup mode*, Int. J. Multiph. Flow **47**, 115 (2012).
[39] V. Sanjay and D. Lohse, *Unifying theory of scaling in drop impact: forces and maximum spreading diameter*, Phys. Rev. Lett. **134**, 104003 (2025).
[40] G. I. Taylor and D. H. Michael, *On making holes in a sheet of fluid*, J. Fluid Mech. **58**, 625 (1973).
[41] Assuming a toroidal initial hole shape [42–45], the excess surface energy $\Delta\Xi$ of a hole of outer radius R can be written as $\dfrac{\Delta\Xi}{\gamma h_0^2} = -\pi + \pi^2\left(\dfrac{R}{h_0}\right) - 2\pi\left(\dfrac{R}{h_0}\right)^2$.
[42] M. Ilton, C. DiMaria, and K. Dalnoki-Veress, *Direct measurement of the critical pore size in a model membrane*, Phys. Rev. Lett. **117**, 257801 (2016).
[43] H. V. Goudarzi, Ph.D. thesis, Sorbonne Université, 2023.
[44] J. A. Moriarty and L. W. Schwartz, *Dynamic considerations in the closing and opening of holes in thin liquid films*, J. Colloid Interface Sci. **161**, 335 (1993).
[45] A. Sharma and E. Ruckenstein, *Energetic criteria for the breakup of liquid films on nonwetting solid surfaces*, J. Colloid Interface Sci. **137**, 433 (1990).
[46] J. M. Kolinski, L. Mahadevan, and S. M. Rubinstein, *Drops can bounce from perfectly hydrophilic surfaces*, Europhys. Lett. **108**, 24001 (2014).
[47] M. Avila, D. Barkley, and B. Hof, *Transition to turbulence in pipe flow*, Annu. Rev. Fluid Mech. **55**, 575 (2023).
[48] D. Samanta, Y. Dubief, M. Holzner, C. Schäfer, A. N. Morozov, C. Wagner, and B. Hof, *Elasto-inertial turbulence*, Proc. Natl. Acad. Sci. USA **110**, 10557 (2013).
[49] J. Eggers, *The subtle dynamics of liquid sheets*, J. Fluid Mech. **672**, 1 (2011).
[50] C. Wang, L. Yang, and H. Ye, *Nonlinear dual-mode instability of planar liquid sheets*, J. Fluid Mech. **778**, 621 (2015).
[51] K. Matsuuchi, *Modulational instability of nonlinear capillary waves on thin liquid sheet*, J. Phys. Soc. Jpn. **37**, 1680 (1974).
[52] C. Mehring and W. A. Sirignano, *Nonlinear capillary wave distortion and disintegration of thin planar liquid sheets*, J. Fluid Mech. **388**, 69 (1999).
[53] H. B. Squire, *Investigation of the instability of a moving liquid film*, Br. J. Appl. Phys. **4**, 167 (1953).